Title	Thermal transient test and strength evaluation of a tubesheet structure made of Mod.9Cr-1Mo steel. Part I: Test model design and experimental results
Author(s)	Masanori Ando, Shinnichi Hasebe, Sumio Kobayashi, Naoto Kasahara, Akira Toyoshi, Takahiro Ohmae and Yasuhiro Enuma
Citation	Nuclear Engineering and Design, 275, p.408-421.
Text Version	Author
URL	http://jolissrch-inter.tokai-sc.jaea.go.jp/search/servlet/search?5042471
DOI	http://dx.doi.org/10.1016/j.nucengdes.2014.04.032
Right	NOTICE: This is the author's version of a work that was accepted for publication in Nuclear Engineering and Design. Changes resulting from the publishing process, such as peer review, editing, corrections, structural formatting, and other quality control mechanisms, may not be reflected in this document. Changes may have been made to this work since it was submitted for publication. A definitive version was subsequently published in Nuclear Engineering and Design, VOLUME 275, 2014, DOI: 10.1016/j.nucengdes.2014.04.032. ©2014 Elsevier B.V. All rights reserved.

Title

Thermal transient test and strength evaluation of a tubesheet structure made of Mod.9Cr-1Mo steel. Part I: Test model design and experimental results

Authors

Masanori Ando

Japan Atomic Energy Agency, Oarai-cho, Higashi-ibaraki, Ibaraki, 311-1393, Japan

ando.masanori@jaea.go.jp

TEL; 8129-267-4141, FAX;8129-266-3675

Shinnichi Hasebe

Japan Atomic Energy Agency, Oarai-cho, Higashi-ibaraki, Ibaraki, 311-1393, Japan

hasebe.shinnichi@jaea.go.jp

TEL; 8129-267-4141, FAX;8129-267-2397

Sumio Kobayashi

Japan Atomic Energy Agency, Oarai-cho, Higashi-ibaraki, Ibaraki, 311-1393, Japan

kobayashi.sumio@jaea.go.jp

TEL; 8129-267-4141, FAX;8129-267-2397

Naoto Kasahara

Japan Atomic Energy Agency, Oarai-cho, Higashi-ibaraki, Ibaraki, 311-1393, Japan

(Presently; The University of Tokyo /Hongo, Bunkyo-ku, Tokyo, Japan, 113-8656)

kasahara@n.t.u-tokyo.ac.jp

TEL&FAX ; 813-5841-0247

Akira Toyoshi

Mitsubishi heavy industries, Ltd, Hyogo-ku Kobe, Hyogo, 676-8585, Japan

akira_toyoshi@mhi.co.jp

TEL; 8178-672-5099, FAX ; 8178-672-3435

Takahiro Ohmae

Mitsubishi heavy industries, Ltd, Hyogo-ku Kobe, Hyogo, 676-8585, Japan

takahiro_omae@mhi.co.jp

TEL; 8178-672-3418, FAX ; 8178-672-3435

Yasuhiro Enuma
Mitsubishi FBR systems, Inc., Jingumae, Shibuya-ku, Tokyo, 150-0001, Japan
(Presently; Japan Atomic Energy Agency, Oarai-cho, Higashi-ibaraki, Ibaraki, Japan, 311-1393)
enuma.yasuhiro@jaea.go.jp
TEL; 8129-267-4141, FAX;8129-267-1676

Abstract

The tubesheet structure is one of the components that suffer the most severe loading in fast reactors, and it is one of the most difficult components to design because of such severe operation conditions and its complex three-dimensional structure with an arrangement of numerous penetration holes. In this study, to clarify the failure mode of a semispherical tubesheet structure originally designed for the steam generator in the Japan sodium-cooled fast reactor, a cyclic thermal loading test was performed using a tubesheet model test structure. The tubesheet model made of Mod.9Cr-1Mo steel was subjected to 1,873 cycles of severe thermal transient loads using a large-scale sodium loop, in which sodium heated to 600°C and 250°C was flowed repeatedly with periods for each transient of 2 and 1 h, respectively. After the test, the test model was inspected by performing liquid penetrant testing. Then, observation using a scanning electron microscope and hardness testing were performed to characterize the failure mechanism in the structural model tested under the thermal transient loading with holds at elevated temperature. A thermal-hydraulic analysis was also performed to validate the measured temperature history during the thermal transient. Through these examinations and evaluation with thermal-hydraulic analysis, the manner of failure in the tubesheet under cyclic thermal loading is discussed.

Keywords

Heat-resistant steel, Fatigue, Creep-fatigue interaction, Elevated temperature design

1. Introduction

Mod.9Cr-1Mo steel is a candidate material for the primary and secondary heat transport system components of the Japan sodium-cooled fast reactor (JSFR) (Aoto et al., 2011). However, there is no adequate experience to support the structural integrity of components made of Mod.9Cr-1Mo steel in actual environments. Although Mod.9Cr-1Mo steel is being used as a structural material for fossil-fired power plants, the structural materials in sodium-cooled fast reactors (SFRs) are exposed to unique operating environments including elevated temperatures and sodium exposure during the plant life. Therefore, it is important to understand the failure mode of the structural components under actual operating environments to assess their integrity.

Since creep-fatigue damage is one of the most important failure modes in the design of fast reactors (FRs), many methods for evaluating the creep-fatigue life have been proposed in the area of material testing (Taguchi et al., 1993; Aoto et al., 1994; Takahashi, 2008a, 2008b, 1999; Asayama et al., 2008). Accordingly, the damage assessment methods in the design codes are mainly formulated by the uniaxial material test data, which were obtained at a isothermal temperature under uniaxial mechanical loading in an air environment. In actual the components are subjected to thermal transient loading, however, the creep-fatigue damage is more complicated than in that observed in the material test because of the multiaxial stress conditions, the distribution of temperature in the structure, and the discontinuous configuration. Therefore, several validation tests simulating the actual loading conditions with structural models are indispensable for codification (Ando et al., 2011, 2012a, 2012b, 2013a).

The steam generator (SG) is one of the key components in the design of an SFR. Large-capacity SGs for a reduction in the number of cooling loops, have been pursued in response to the demand for economic competitiveness in design studies of commercial SFRs. The design is complicated because of elevated-temperature effects, high pressure, and the potential for a sodium-water reaction. Therefore, adoption of a once-through sodium-heated SG with double-walled straight tube SG made of Mod.9Cr-1Mo steel has been planned for next-generation FRs in Japan (Chikazawa et al., 2012; Kurome et al., 2010; Futagami et al., 2009). In this SG, the pressure of the outlet steam is planned to be 19.2 MPa with a temperature reaching 497 °C under normal operation. Double-wall straight tubes will be adopted to mitigate the risk of a sodium-water reaction. To achieve economic competitiveness, a large-capacity once-through boiler (over 30 m) has been designed with Mod.9Cr-1Mo steel, because this steel has both excellent thermal properties and adequate high-temperature strength with good stress corrosion cracking resistance. The use of Mod.9Cr-1Mo instead of conventional steel enables a simpler system with a once-through boiler to be designed. In the Monju prototype FR in Japan, the SG was separated into an evaporator (EVA) and a superheater (SH). The EVAs and SHs were made from 2.25Cr-1Mo steel and SUS321 steel, respectively, because of the corrosion effects (Masuura et al., 2007).

To achieve the above design concepts in practice, a new conceptual semispherical tubesheet, called the center-flattened spherical tubesheet (CFST), was designed by the authors (Ando et al., 2013b). This CFST was designed to withstand high temperatures (497.2 °C) with high internal pressures (19.2 MPa) and thermal stress during a thermal transient. A large perforated region design for attaching the numerous straight tubes without significant local peak stress at hole edge during a thermal transient has been achieved by a tubesheet design which combined a flat and a spherical perforated plate. The purpose of the design is to mitigate the stress inducement mechanisms during a thermal transient while maintaining the primary stress below the design limits. To avoid stress concentration at the edges of the holes, the penetration angle of the perforated region was limited to 30 degrees. However, when the penetration angle is maintained below 30 degrees, the plenum volume has to be increased in the semi-spherical tubesheet, which leads to a large peak stress. Therefore, the CFST model adopts a flat plate with a radially perforated area. In fact, adoption of this CFST instead of a conventional flat tubesheet has been planned to accommodate a large-scale high-pressure SG.

This CFST is an original design, and no data to validate its structural integrity are available. Therefore, the main purpose of this study is to identify the failure mode of a CFST subjected to severe cyclic thermal loading. In addition, identification of the location of crack initiation, the distribution of cracks, and the direction of crack propagation is also an important objective of this test, because these attributes may not be simulated accurately in ordinary finite element analysis (FEA). The test data, which were obtained on the temperature distribution in the test model during the test and the crack situation as mentioned above, were supplied to validate the evaluation methods. In fact, it was another motivation for planning this structural test using a large-scale test model.

Since sodium has the large thermal capacity at a low pressure, this strength test was performed in a sodium environment, although real the tubesheet in the actual SGs is used in a steam environment, where water flows from the lower plenum to the upper plenum through the heat exchanger tubes. However, sodium flows from the upper plenum to the penetration holes of the tubesheet in this test, which makes the environment different. Nevertheless, the location of crack initiation, the distribution of cracks, and the direction of the crack propagation were supposed to be simulated accurately in this test, because the failure life in creep-fatigue testing was independent of the environment (Asayama et al., 2001).

At the actual serviced tubesheet in SGs, the failure is supposed to be caused by superposition of the primary stress by internal pressure and the secondary stress by thermal loading. The primary stress raises the base stress and secondary stress generates the stress amplitude during a thermal transient. The primary stress level and the stress amplitude by secondary stress depend on the situation of the thermal transient and the operation sequence. It means that the important stress inducement mechanism for the failure evaluation is secondary. Therefore, the examination result subjected to the simplified thermal loading is very useful to investigate the failure mechanism of the semi-spherical tubeseet. In fact, the stress inducement mechanism in the test model was comparable to that of a CFST, because the mechanism in the CFST under the thermal transition was analyzed and considered in the design of the test model (Ando et al., 2013b).

2. Thermal transient test

2.1 Configuration of the test model

The test model was made of Mod.9Cr-1Mo steel and designed as a tubesheet structure simulating the stress inducement mechanism of the CFST. Illustrations and specifications of the CFST adopted in JSFR are shown in Fig. 1. The test model of the tubesheet structure was designed considering the stress inducement mechanism in the CFST, the test capacity of the TTS (Thermal Transient Test Facility for Structures), acquirable forged material, and the testing time. In particular, the stress inducement mechanism was adjusted as the superposition of the gross hoop stress and the local stress concentrated at the edges of the outer-layer holes in the test model design. One of the thermal stress mechanisms in the CFST is hoop stress inducement caused by interaction between the perforated and surrounding regions. When a thermal transient occurs, the temperature of the perforated region quickly responds to the fluid temperature through the attached numerous tubes. On the other hand, in the surrounding regions, which are the rim and shroud, the temperature response is slow. Consequently, the surrounding regions do not contract as much as the perforated region. Therefore, this mechanism originates from the difference in the temperature responses and induces hoop stress. The other thermal stress mechanism of tubesheet is peak stress inducement caused by the stress concentration around the edges of the holes in the perforated region, especially locates at high penetration angle. Therefore stiffness balance of tubesheet and surrounding regions were adjusted to simulate such thermal stress inducement mechanism and the maximum penetration angle in the perforated region of the test model was limited to 30°. These fundamental features conformed to the specifications of the CFST. Based on these fundamental concepts, the detailed design of the test model was defined using FEA to generate a comparable stress inducement mechanism and appropriate creep-fatigue damage in the test section of the tubesheet under the assumed thermal loading conditions. A hole diameter of 19.2 mm and a pitch of 40.0 mm with a triangle penetration pattern were also adopted in the test model design. The number of penetration layers was constrained by the maximum size of the raw material available. An outline summary of the dimensions is given in Fig. 2.

In addition to the test section of the tubesheet, an upper plenum and a lower plenum with nozzles for the thermocouples were designed. A nozzle for microscope inspection was also equipped in the upper plenum. This nozzle was equipped to allow the cracking to be checked when the test was interrupted. On the top end of the upper plenum, a sodium inlet nozzle was equipped, and it was connected to a test structure of the thick cylinder model. In fact, two test models were tested at the same time. This thick cylinder model was tested for the purpose of the confirming the fracture mode and validating the failure evaluation methods in a simple structural model. In addition, this test was expected to contribute to the understanding of the test results obtained for the tubesheet structure. The test results for the thick cylinder model were reported in a previous paper (Ando et al., 2013a). The total height of this test model was 3,500 mm, the width was 750 mm, and it was composed of five plenums and five nozzles. The chemical compositions and mechanical properties are summarized in Table 1. All of the ingots were cast from the same batch, although the heat treatments were different. The test model was machined from the several forged material ingots shown in Table 2. Table 2 shows the configurations and the thermal treatments. In order to form a uniform microstructure with the specified mechanical strength, F1, F2, and F4 in Table 2 were partially hollowed out. The normalization and tempering times were accommodated, taking into account the configurations. All of the parts, plenum, tubesheet, and nozzles, were connected using gas tungsten arc welding.

2.2 Measurements

To measure the temperature distribution, alumel-chromel–type thermocouples were attached at 89 points. The measured points are summarized in Fig. 3. On the tubesheet section, thermocouples were attached at 26 points to measure the local temperature distribution. The sodium temperature was also measured by thermocouples located on the sodium flow line at 13 points. In addition to these, thermocouples were attached to 27 points on the rims of the tubesheet and on the inner side of the plenums. The temperature distribution of the outer side of test model was also measured at 23 points.

Magnetic flow meters were used to measure the flow rates of the elevated-temperature sodium for both the hot and cold circuits, and the total of these was adjusted to a constant rate of 100 L/min during the test. Controlling the power of the electromagnetic pumps equipped for the hot and cold circuits enabled a constant sodium flow to be supplied into the test model.

2.3 Test facility and test conditions

A large-scale sodium test loop named the TTS at the Oarai Engineering Center of the Japan

Atomic Energy Agency was used (Nakanishi et al., 1985) in this study. The TTS has two independent sodium loops: a hot sodium circuit with an electric heater and a cold circuit with an air-cooler. The electromagnetic pumps installed in each circuit drive 600 °C and 250 °C sodium and can mix them in any proportion (Kawasaki et al., 2007, 2008). The TTS equipment was modified to perform this test, since Mod.9Cr-1Mo steel has excellent thermal load resistance.

Hot and cold sodium were supplied from the mixing tee attached to the thick cylinder test model (Ando et al., 2013a), and uniformly mixed sodium flowed into the upper plenum thorough the inlet nozzle at a constant flow rate of 100 L/min. For the hot transient, sodium heated to 600 °C was led into the test model, and a constant sodium flow was maintained for 2 h. For the cold transient, sodium heated to 250 °C was led into the test model, and a constant sodium flow was maintained for 1 h. A 2 h with hold at 600 °C after the hot transient was chosen to generate creep damage due to stress relaxation. A 1 h hold at 250 °C after the cold transient was chosen to eliminate the temperature distributions in the test model and the TTS components for the following cycle. The electromagnetic pumps installed in each circuit enabled the temperature change rate of the flowing sodium to be controlled to 5 °C/s. As a result, it took 3 h and 140 s for a cycle. The sodium temperature history measured at the inlet nozzle (UE-N-01-φ in Fig. 3) is shown in Fig. 4. The oxygen density was suppressed to low levels of 6 ppm in the sodium loop. A total of 1,873 thermal transient cycles scheduled were applied to the test model.

3. Test results

3.1 Measured results of the temperature transition

The repeatability of the temperature histories was good for all 1,873 cycles. The measured temperature histories of the sodium near the tubesheet section are shown in Fig. 5. During the hot transient shown in Fig. 5(a), the temperature increased from the top downward. The temperatures measured at the center of test model, at TU-N-01-φ and TL-N-01-φ, had a small peak about 50 s after the start of the hot transient in the temperature transition history. In addition, a smaller peak was also observed after about 50 s at TL-N-01-C.

In contrast, the rates of temperature decrease at the center of test model, at TU-N-01-φ and TL-N-01-φ, were larger than those measured at the upper side, at TU-N-01-C and TU-N-02-C, in the initial stage of the cold transient. After about 100 s had elapsed from the start of the cold transient, the temperature changes at the center of test model were interrupted for 50 s. Then, because of this break in the temperature change at the center of the test model, at TU-N-01-φ and TL-N-01-φ, the temperature change at TU-N-01-φ became similar to those at the upper side. In contrast, the temperature change at the lower side of the center of the tubesheet, at TL-N-01-φ, became similar to those at the lower side.

3.2 Results of the liquid penetrant testing

After 1,873 cycles of the thermal transient test, the test model was removed from the TTS. Then, the test model was inspected by performing liquid penetrant testing (PT) on the outer surface and was cut to perform PT on the inner surface. No cracks were observed on the inner or outer sides of the test model, except at the hole edges of the tubesheet. Half of the tubesheet section was cut into small pieces so that the cracking of the inner surface of the penetration holes could be observed. An outline of the separation of the test model and the identification numbers assigned to each hole are shown in Fig. 6.

Many cracks were observed by PT on the upper surface of the tubesheet and on the inner surfaces of the penetration holes. Several results are shown in Fig. 7. In this figure, the observed cracks are traced by red lines for clarification. The colored parts near the hole in Fig. 7 are debris of the strips used to fix the thermocouples. These strips were spot-welded to the test model and were not removed completely to avoid scratching the damaged area.

Since the penetration holes were arranged in a triangle pattern, the holes were located geometrically similarly every 30°. This means that A1 and A2 had mirror symmetry with respect to the meridional axis passing through the center of the tubesheet in Fig. 6, although the observed cracks were not completely mirror symmetric.

Many short cracks were observed at the hole edges, and 372 cracks were observed on the upper surface of the tubesheet by PT. It was assumed that these cracks propagated radially outward from the hole edge. Most crack lengths were shorter than 2.0 mm, but 33 cracks propagated over 2.0 mm on the surface. The maximum crack length on the upper surface was 4.15 mm for B1, and this crack was propagating in the 50° direction in Fig. 6. However, the crack length in the thickness direction was 0.78 mm. On the other hand, 37 cracks were measured on the inner surfaces of the penetration holes, and 4 of these cracks exceeded 2.0 mm. The maximum crack length was 3.70 mm for A2, and this crack was located at 135° in Fig. 6. The sum of the crack lengths on the upper and inner surfaces was the longest for this crack.

All of the observed crack data are superimposed on a figure showing the 30° sections, because the holes were located geometrically similarly every 30°. The superimposed figure is shown in Fig. 8. It is evident that cracks were concentrated at the outermost layer holes (*a* and *d* in Fig. 8) and at the hole in the second outermost layer (*c* in Fig. 8). It had been forecasted that the outer-layer hole edge would be likely to failure because this test model was designed to simulate semi-spherical tubesheet. In fact, these situations indicated that the plan to simulate the stress inducement mechanism of the CFST was successful.

This crack distribution appears to show that the cracks propagated from the each hole edge toward the nearest hole. In other words, the cracks that initiated at the edge of the outermost hole *d* propagated toward the mirror-symmetric hole *d* and hole *c*.

3.3 Scanning electron microscope observation results

Microstructural observation was performed using an optical microscope (OM) and a scanning electron microscope (SEM). For the OM observation, the surface was etched using an inverse aqua-regia to reveal the general structure. An OM image of a crack on the upper surface is shown Fig. 9. It is apparent that the material had an ordinary tempered martensitic structure, and the main crack did not propagate straightly in Fig. 9. For the other cracks, a similar winding path with several branches was also observed. The relationship between the crack path and the prior austenite grain boundary or packet boundary of the material could not be confirmed clearly. These features were similar to those observed for the thick cylinder model (Ando et al., 2013a).

In order to observe the failure surface using a SEM, holes A2 and F9 were cut out and t forcibly opened. The observed failure surfaces of F9 are shown in Fig. 10. In a region of failure surface near the crack initiation point (F9-a in Fig. 10), a dimple-like deformation with many tiny convex structures was observed. On the other hand, striations associated with cyclic loading were observed near the end-point of the crack (F9-b in Fig. 10). These features of the cracks were also similar to those observed for the thick cylinder model (Ando et al., 2013a).

3.4 Vickers hardness test

Vickers hardness tests were performed to confirm the softening due to cyclic thermal loading. The tests were performed along the line connecting the centers of holes E1 and F1, which corresponds to the line connecting *h* and *e* in Fig. 8. To validate the relationship between the depth from the upper surface and the hardness, the discrete tubesheet section was additionally cut into a smaller piece. The processing procedure for the hardness testing and the locations are shown in Fig. 11, along with the results of the hardness test. For each line, the hardness was measured at 14 points with a 0.5 mm pitch using a 1,000 g weight. The measured hardness slightly increased with the distance from the hole edge in all sections. The hardness near the hole edge was approximately HV180 in sections 1 and 2. The minimum hardness was measured at the nearest point in all sections. On the other hand, the results of the hardness test on the upper surface around holes A1, B1, and D9 were HV180–HV190, and these results were independent of the distance from the hole edges. In addition, the results of the hardness test on the surface along the depths of penetration holes B5 and D1 were also HV180–HV190 and showed no depth dependence. This indicates that the hardness on the surface was uniformly decreased owing to the cyclic thermal loading at the elevated temperature. These results are similar to that obtained in the thick cylinder test (Ando et al., 2013a)

4. Thermal-hydraulic analysis

4.1 Finite-volume analysis model

In order to determine the reason behind the character of the temperature transition during the test shown in Fig. 5, thermal-hydraulic analysis was performed using the ANSYS CFX, with a shear stress transport model. The model used for the finite-volume analysis (FVA) is shown in Fig. 12. A three-dimensional FVA model with 30° sectors was used because the holes were located geometrically similarly every 30°. The detailed geometry of the volume filled by the sodium and the transition conditions applied were shown in Fig. 2 and described in section 2.2, respectively. For the analysis model, the solid elements of ANSYS CFX were utilized. The material properties of the sodium were obtained from the JSME Data Book (JSME, 2009). In the FVA, for simplicity, the boundary condition was assumed to be adiabatic with free slipping on the contact surface of the test model.

4.2 Thermal hydraulic analysis results

The calculated temperature histories at the locations corresponding to those indicated in Fig. 5 are shown in Fig. 13. In Fig. 13(a), small peaks are found after around 20 s at the center of the model, at TU-N-01-φ and TL-N-01-φ. In addition to these, a smaller peak was also found at TL-N-01-C. This character of the simulated temperature transition matches the experimental results shown in Fig. 5 well. However, the peak time and temperature data do not exactly agree with the experimental values because of the simple boundary conditions used.

On the other hand, in Fig. 13(b), the rate of temperature decrease at the center of the model, at TU-N-01-φ and TL-N-01-φ, changed at around 70 s. This rate change was not clear at the other locations shown in Fig. 13(b). This tendency agrees with that in the experimental results, although the temperature decrease was interrupted in the experimental result. Qualitatively, adequate simulation of the thermal transition history in the test was achieved.

As a result, it is concluded that the characters of the temperature history during the hot and cold transients were caused by the nature of this test, not the TTS facility or measurement systems.

5. Discussion

5.1 Failure mechanism

Several design studies on semispherical tubesheets have been proposed (Pratt and Pritchard, 1983; Griffin, 1985; Kumar et al., 2007). However, there has been little consideration of the stress inducement mechanism and design procedure for semispherical tubesheet, and thus they are known with little certainty. Since recent calculation methods and computer development have made it possible to calculate the stress response to the thermal transient of a complex three-dimensional tubesheet design with a large-scale FEA model, the authors proposed a design for stress mitigation for the CFST by considering the thermal stress inducement mechanism (Ando et al., 2013b). It has been planned to adopt the proposed CFST as the tubesheet of the steam generator of the JSFR. Although FEA serves as a powerful tool for tubesheet design, it is difficult to predict the generation and propagation of cracks in the tubesheet. The data on the crack generation and propagation and the failure surface photographs obtained in this test are very important for discussion of the structural integrity of the semispherical tubesheet. The observations of the cracks shown in Fig. 7 indicate that not just one main crack is initiated and propagated at the point of maximum induced stress. In fact, several cracks are initiated around the hole edge and propagate radially under the test conditions. The cracks propagate radially outward from the hole edge mostly in the direction connecting the hole center and that of the nearest hole, as shown in Fig. 8. Around hole *c* in Fig. 8, several cracks propagated toward holes *a* and *g*. The crack distributions around holes *a*, *c*, *d*, *e*, *f*, and *g* suggest that the cracks rarely initiated and propagated toward the outer side of the tubesheet. The features of the crack propagation path, shown in Fig. 9, are similar to those obtained for the thick cylinder model (Ando et al., 2013a).

The number of cracks counted on the upper surface of the tubesheet section of the test model was larger than the number counted on the inner surfaces of the penetration holes. However, the observation of the forcibly opened crack suggested that crack was initiated at the surface of the penetration hole. To clarify the crack initiation and propagation process, the observations of A2 are summarized in Fig. 14. On the forcibly opened failure surface of A2, an area where the failure surface was chewed up and scraped was observed near the penetration hole surface. Striations were observed inside of the crack, and the direction of crack propagation is also summarized in Fig. 14. In addition, an area where striation was not clearly observed was located near the upper surface of the tubesheet.

These results suggest that the main crack was initiated at the inner surface of the penetration hole, very near the upper surface of the tubesheet. Then, it propagated to the upper surface of the tubesheet. This surface analysis suggests that the area near the upper surface of the tubesheet was relatively creep-damaged, and when crack was initiated, it propagated naturally in this area. The uniform softening of the material on the upper surface of the tubesheet and the results of thick cylinder test support this assumption (Ando et al., 2013a).

These results indicate that the failure mode of the tubesheet model was creep-fatigue interaction and it initiated the cracks at the inner surface of the penetration hole, very near the upper surface of the tubesheet. In conclusion, it can be suggested that the failure mode of CFST is the similar as that of the above-mentioned phenomena.

Since this kind of the experimental result on the crack initiation and propagation of a perforated plate has been little reported, these results will support further investigations of the tubesheet design and considerations of the structural integrity.

5.2 Thermal hydraulics during the test

Controlling the thermal transient conditions to perform cyclic thermal loading tests has been difficult, especially using a structural model. The authors have a great deal of experience in adjusting the required test conditions using the long experience with the TTS. A complex waveform of the thermal transient can also be supplied for the test (Kawasaki et al., 2007, 2008). For this test, a custom-designed mixing tee was used to supply uniform-temperature sodium (Ando et al., 2013a). The adequacy of the sodium flow supplied to the test model was confirmed by a temperature adjustment pretest with a mockup test model. However, the measured temperature history was difficult to understand in the test. In particular, there were small temperature peaks during the hot transient and changes in the rate of temperature decrease during the cold transient. These characteristics of the temperature history were simulated well using FVA. Detailed analysis of the FVA results suggested that these characteristics were caused by approach of the stream to the upper surface of the tubesheet. A series of the FVA results for the 0° section, corresponding with the section in Fig. 6, is shown in Fig. 15.

During the hot transient, elevated-temperature sodium flowed into the stagnant sodium at 250 °C. The streamline with temperature contours at 40 s in Fig. 15 shows that the sodium temperature around the center of tubesheet was elevated by the direct stream before the outer side area was heated. Then, the stream directly approaching the upper surface of the tubesheet nearly disappeared because of the buoyancy force. This initial direct stream approaching the upper surface and its subsequent disappearance caused the small peak in the thermal history of the sodium temperature around the center of the tubesheet. After 120 s, the direct stream approaches the upper surface of the tubesheet again, and the flow reaches a steady state. These processes cause the characteristics of the temperature history during the hot transient shown in Fig. 5(a).

On the other hand, during the cold transient, lower temperature sodium flowed into the stagnant sodium at 600 °C. The lower temperature sodium approached the upper surface of the tubesheet uniformly. However, the temperature of sodium passing the outer side penetration holes was raised by the elevated-temperature sodium that entered the upper plenum before this transient. This heat transfer from the sodium caused a relatively larger decrease in the sodium temperature around the center of tubesheet than around the outer side. As time passes, the difference in sodium temperature between the center of the tubesheet and around the outside becomes smaller.

As a result, the characteristics of the sodium temperature history measured during the hot and cold transients were attributed to the characteristics of the direct stream of inflowing sodium. To reduce the effect of the direct stream, a larger ratio of the distance from the inlet nozzle to the tubesheet and the inside diameter of the inlet nozzle should be applied. In this study, it was about 8, 495.5 mm/62.3 mm, because only the length of a theoretical potential core was considered. As an alternative idea, a model design with an inhibitor plate interrupting the direct stream in the upper plenum is recommended.

6. Conclusion

A cyclic thermal loading test of a tubesheet model made of Mod.9Cr-1Mo steel was successfully conducted using a large-scale sodium loop. To investigate the character of its failure mode under cyclic thermal loading with a given holding time at elevated temperature, PT, Vickers hardness testing, and observation of failure surface were performed. Moreover, thermal hydraulics analysis was performed to clarify the reasons for the characteristics of the sodium temperature history measured during the test. These results can be summarized as the following points:

(1) The SEM observation clarified that failure mode was creep-fatigue and which generated the cracks from the inner surface of the penetration hole near upper surface of tubesheet. Then, these propagated toward the upper surface of the tubesheet. This mechanism was also supported by the results of the hardness test.

(2) The observed crack initiation and propagation in the tubesheet model simulating the CFST clarified that a number of cracks were initiated around the edges of holes in the outermost layer and in the second outermost layer, and these cracks propagate radially.

(3) The PT test indicated that cracks propagated mostly in the direction of the line connecting each hole edge to the nearest hole. In contrast, cracks rarely initiated and propagated toward the outer side of the tubesheet.

(4) The measured temperature history and thermal hydraulics analysis indicated that the temperature histories during the thermal transients were caused by the direct stream of inflowing sodium approaching the upper surface of the tubesheet.

Acknowledgement

This paper includes the results of the “Technical development program on a commercialized FBR plant” entrusted to the Japan Atomic Energy Agency (JAEA) by the Ministry of Economy, Trade and Industry of Japan (METI). The authors wish to express their gratitude for the enthusiastic efforts in the design and fabrication of the test model by Mr. Usui and co-workers of Mitsubishi Heavy Industry, Ltd. The authors are grateful to Mr. Osamu Inoue of IX Knowledge, Inc., for performing the FVA.

Reference

- Ando, M., Hasebe, S., Kobayashi, S., Kasahara, N., Toyoshi, A., Ohmae, T., Enuma, Y. Thermal transient test and strength evaluation of a thick cylinder model made of 2013a, Mod.9Cr-1Mo steel, Journal of Nuclear Engineering and Design, No.255, pp.296-309
- Ando, M., Hirose, Y., Date, S., Watanabe, S., Enuma, Y., Kawasaki, N. 2012a, Verification of the estimation methods of strain range in notched specimens made of Mod.9Cr-1Mo, Journal of pressure vessel technology, Vol.134, pp.61403-1 - 61403-12
- Ando, M., Hirose, Y., Karato, T., Watanabe, S., Inoue, O., Kawasaki, N., Enuma, Y. 2011, Comparison of Creep-fatigue evaluation methods with notched specimens made of Mod.9Cr-1Mo steel", Proceedings of ASME Pressure Vessel and Piping Conference 2011, PVP2011-57532, 2011
- Ando, M., Kanasaki, H., Date, S., Kikuchi, K., Sato, K., Takasho, H., Tsukimori, K. 2012b, A study on fatigue and creep-fatigue life assessment using cyclic thermal tests with Mod.9Cr-1Mo steel structures, Proceedings of ASME Pressure Vessel and Piping Conference 2012, PVP2011-78042
- Ando, M., Takasho, H., Kawasaki, K., Kasahara, N. 2013b, Stress mitigation design of tubesheets with consideration of thermal stress inducement mechanism, Journal of Pressure Vessel Technology, Vol.135, Issue 6, pp.061207-1-061207-10
- Aoto, K., Komine, R., Ueno, F., Kawasaki, H., Wada, Y. 1994, Creep-fatigue evaluation of normalized and tempered Modified 9Cr- 1Mo", Journal of Nuclear Engineering and Design, No.153, 1994, pp.97-110
- Aoto, K., Uto, N., Sakamoto, Y., Ito, T., Toda, M., Kotake, S. 2011. Design Study and R&D Progress on Japan Sodium-Cooled Fast Reactor. Journal of Nuclear Science and Technology 2011, Vol.48, pp.463-471
- Asayama, T. and Jetter, R. 2008, An overview of creep-fatigue damage evaluation methods and an alternative approach, Proceedings of ASME Pressure Vessel and Piping Conference 2008, ASME PVP2008-61820
- Chikazawa, Y., Aoto, K., Hayafune, H., Kotake, S., Ohno, Y., Ito, T., Toda, M., 2012, Evaluation of JSFR Key Technologies, Nuclear Technology, Vol.179, No.3, pp. 360-373
- Futagami, S., Hayafune, H., Fujimura, K., Sato, M., 2009, A Study on LMFBR steam generator design without tube failure propagation in water leak events, Proceedings of 2009 International Congress on Advances in Nuclear Power Plants (ICAPP '09), pp1419-1428
- Griffin, D.S. 1985, Elevated-temperature structural design evaluation issue in LMFBR licensing", Nuclear Engineering and Design, Vol.90, pp.299-306

- Japanes society of mechanical engineers, 2009,JSME Data Book : Heat transfer 5th edition, Maruzen, Tokyo
- Kawasaki, N., Hasebe, S., Kobayashi, S., Kasahara, N. 2007, SPECTRA Thermal Fatigue Tests Under Frequency Controlled Fluid Temperature Variation: Strength Tests, Proceedings of ASME Pressure Vessel and Piping Conference 2007, ASME PVP2007-26414
- Kawasaki, N., Takasho, H., Kobayashi, S., Hasebe, S., Kasahara, N. 2008, Spectra Thermal Fatigue Tests Under Frequency Controlled Fluid Temperature Variation: Superposed Sinusoidal Temperature Fluctuation Tests, Proceedings of ASME Pressure Vessel and Piping Conference 2008, ASME PVP2008-61225
- Kumar, R.S., Srinivasan, R., Chellapandi, P., Chetal, S.C. 2007, Theoretical explanation for acceptability of steam generator tubesheet shell junction under manufacturing deviation" 19th International Conf. on Structural Mechanics in Reactor Technology, F04/4
- Kurome, K., Murakami, H., Tsujita, Y., Futagami, S., Hayafune, H., 2010, Development of the main components for JSFR, Proceedings of 2010 International Congress on Advances in Nuclear Power Plants (ICAPP '10), pp.637-644
- Masuura, M.,Hatori, M., Ikeda, M., 2007, Design and modification of steam generator safety system of FBR MONJU Original Research Article, Nuclear Engineering and Design, Vol.237, pp.1419-1428
- Nakanishi, S., Watashi, K., Kanazawa, S., Aoki, T., Imazu, A., Kano, T., Ishizaki, K. 1985, Thermal transient test facility for structures, Transactions of the 8th International Conference on Structure Mechanics in Reactor Technology(SMiRT-8), Vol.E, pp.37-42
- Pratt. R, Pritchard, O. J., 1983, The design of dished tubeplates using the equivalent plate models, Transaction of 7th International Conference on Structural Mechanics in Reactor Technology, E3/8, pp.149-156
- Taguchi, K., Ueta, M., Dozaki, K., Sukekawa, M., Kato, H., Asada, Y. 1993, Creep-fatigue life prediction for modified 9Cr-1Mo steel, Proceedings of ASME Pressure Vessel and Piping Conference 1993, PVP-Vol.262, pp.175-180
- Takahashi, Y. 2008a, Study on creep-fatigue evaluation procedures for high-chromium steels-Part I: Test results and life prediction based on measured stress relaxation, International Journal of Pressure Vessels and Piping, Vol. 85, pp.406-422
- Takahashi, Y. 2008b, Study on creep-fatigue evaluation procedures for high chromium steels - Part II: Sensitivity to calculated deformation", International Journal of Pressure Vessels and Piping, Vol. 85, pp.423-440
- Takahashi, Y., 1999. Further evaluation of creep-fatigue life prediction methods for low-carbon nitrogen-added 316 stainless steel, J. Pres. Ves. Technol. 121, 142-148.

Table Lists

Table 1

(a) Chemical composition (weight %)

C	Si	Mn	P	S	Ni	Cr	Mo	Nb	V	Al	N
0.11	0.31	0.44	0.008	0.001	0.17	9.17	0.97	0.07	0.22	0.01	0.044

(b) Mechanical properties

Material	0.2% offset yield strength (MPa)	Tensile strength (MPa)	Elongation (%)	Reduction of area (%)
F1	497	656	25.9	66.5
F2	548	681	23.6	69.7
F3	482	632	25.6	68.2
F4	478	643	26.9	65.7
F5	495	652	26.0	71.0

Table 2

<table>
<tr><th rowspan="2"></th><th rowspan="2">Application</th><th rowspan="2">Configuration</th><th colspan="2">Thermal treatment</th></tr>
<tr><th>Normalizing</th><th>Tempering</th></tr>
<tr><td>F1</td><td>Upper plenum</td><td rowspan="2">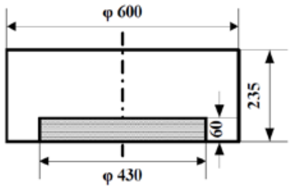

Hollowing for thermal treatment</td><td rowspan="2">1060 °C - 8 h AC</td><td rowspan="2">770 °C - 10 h AC</td></tr>
<tr><td>F2</td><td>Lower plenum</td></tr>
<tr><td>F3</td><td>Middle plenum for both end of the tubesheet (Separated into 2 parts)</td><td>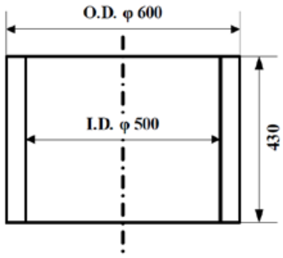
</td><td>1060 °C - 3.5 h AC</td><td>770 °C - 5.5 h AC</td></tr>
<tr><td>F4</td><td>Tubesheet</td><td>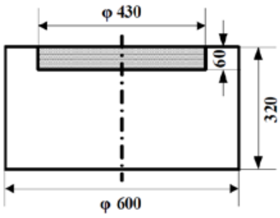

Hollowing for thermal treatment</td><td>1060 °C - 11.5 h AC</td><td>770 °C - 12.5 h AC</td></tr>
<tr><td>F5</td><td>Nozzles</td><td>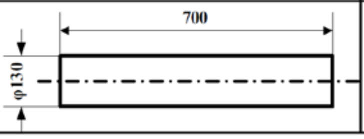
</td><td>1060 °C - 8 h AC</td><td>770 °C - 10 h AC</td></tr>
</table>

AC; Air cooling

List of figures

Fig.1

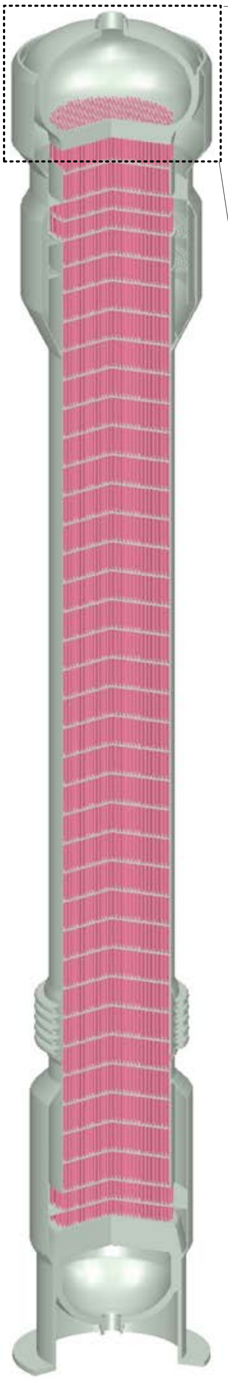

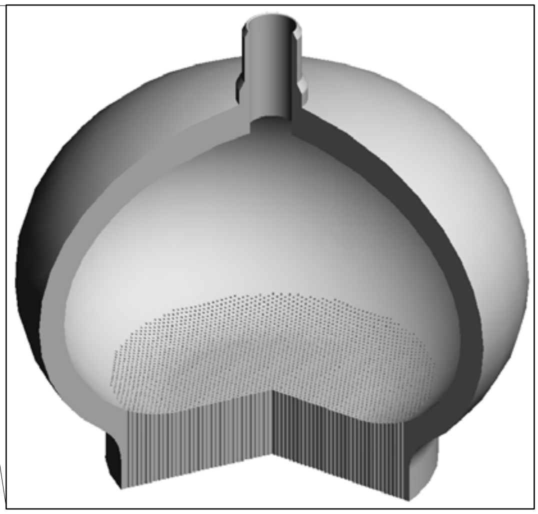

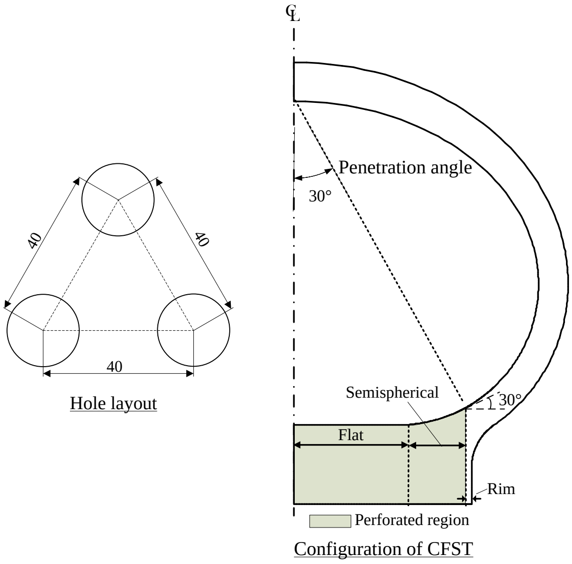

Specification of CFST

Item	Unit	Value
Number of tube		4010
Tube outer diameter (inner tube / outer tube)	mm	15.6 / 19.0
Tube thickness (inner tube / outer tube)	mm	1.4 / 1.7
Tube pitch (Triangular)	mm	40
Material	Mod.9Cr-1Mo steel	

Unit : mm

Fig.2

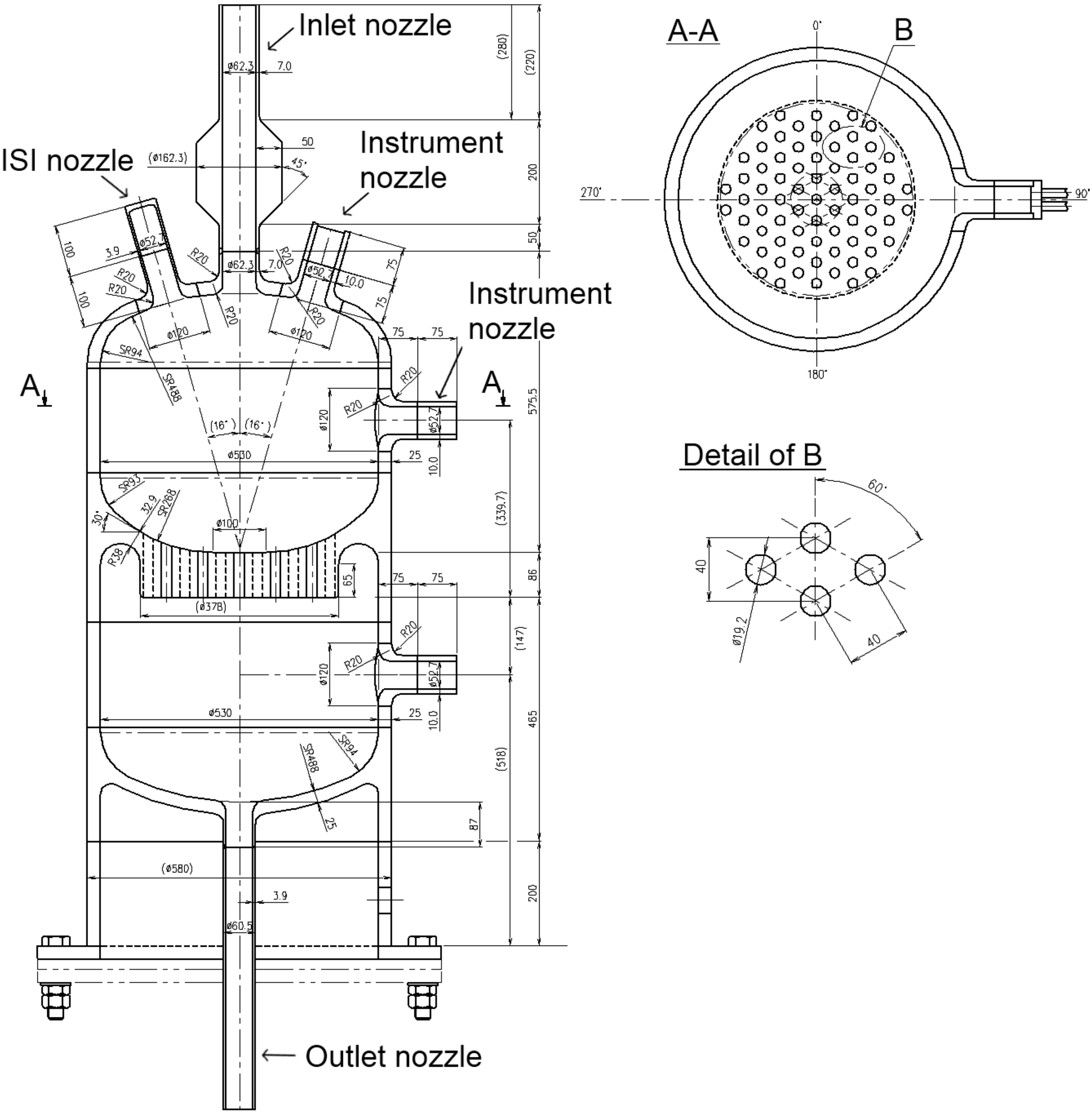

Inlet nozzle
ISI nozzle
Instrument nozzle
Instrument nozzle
Outlet nozzle
A-A
B
Detail of B

Fig.3

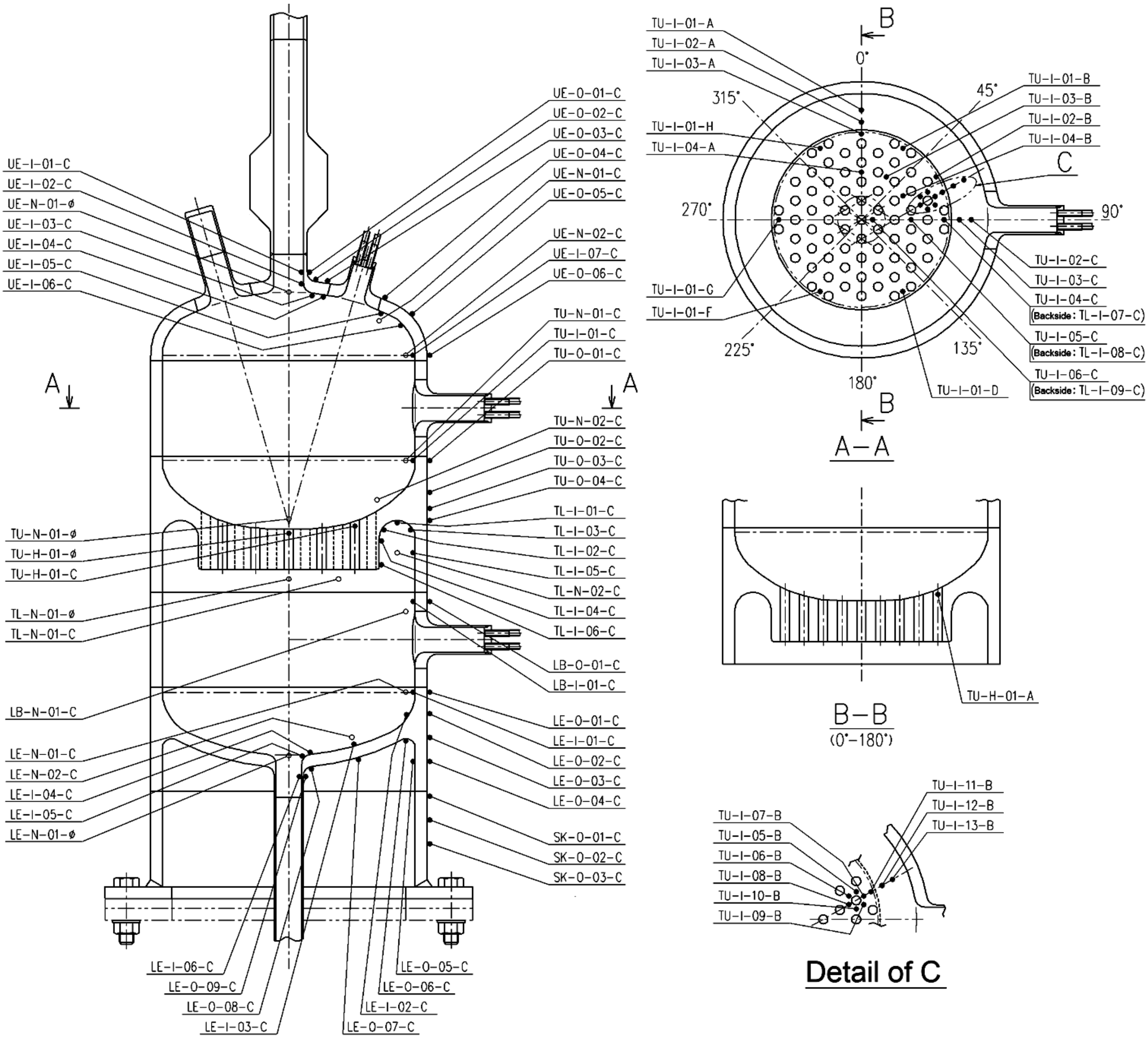

UE-O-01-C
UE-O-02-C
UE-O-03-C
UE-O-04-C
UE-N-01-C
UE-O-05-C
UE-I-01-C
UE-I-02-C
UE-N-01-ø
UE-I-03-C
UE-I-04-C
UE-I-05-C
UE-I-06-C
UE-N-02-C
UE-I-07-C
UE-O-06-C
TU-N-01-C
TU-I-01-C
TU-O-01-C
A
A
TU-N-02-C
TU-O-02-C
TU-O-03-C
TU-O-04-C
TL-I-01-C
TL-I-03-C
TL-I-02-C
TL-I-05-C
TL-N-02-C
TL-I-04-C
TL-I-06-C
TU-N-01-ø
TU-H-01-ø
TU-H-01-C
TL-N-01-ø
TL-N-01-C
LB-O-01-C
LB-I-01-C
LB-N-01-C
LE-O-01-C
LE-I-01-C
LE-O-02-C
LE-O-03-C
LE-O-04-C
LE-N-01-C
LE-N-02-C
LE-I-04-C
LE-I-05-C
LE-N-01-ø
SK-O-01-C
SK-O-02-C
SK-O-03-C
LE-I-06-C
LE-O-09-C
LE-O-08-C
LE-I-03-C
LE-O-05-C
LE-O-06-C
LE-I-02-C
LE-O-07-C
TU-I-01-A
TU-I-02-A
TU-I-03-A
B
0°
315°
45°
TU-I-01-B
TU-I-03-B
TU-I-02-B
TU-I-04-B
C
TU-I-01-H
TU-I-04-A
270°
90°
TU-I-02-C
TU-I-03-C
TU-I-04-C
(Backside: TL-I-07-C)
TU-I-01-G
TU-I-01-F
TU-I-05-C
(Backside: TL-I-08-C)
225°
135°
TU-I-06-C
(Backside: TL-I-09-C)
180°
TU-I-01-D
B
A−A
TU-H-01-A
B−B
(0°−180°)
TU-I-11-B
TU-I-12-B
TU-I-13-B
TU-I-07-B
TU-I-05-B
TU-I-06-B
TU-I-08-B
TU-I-10-B
TU-I-09-B
Detail of C

Fig.4

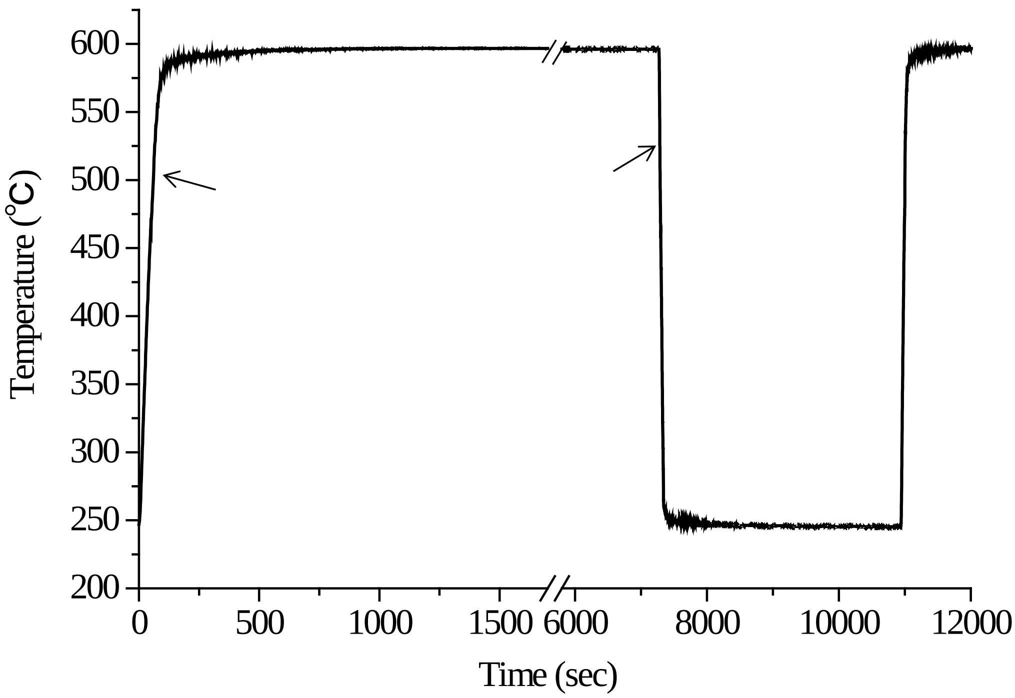
600
550
500
450
400
350
300
250
200
Temperature (℃)
0
500
1000
1500
6000
8000
10000
12000
Time (sec)

Fig.5

(a) 0 sec ～ 700 sec / hot transient

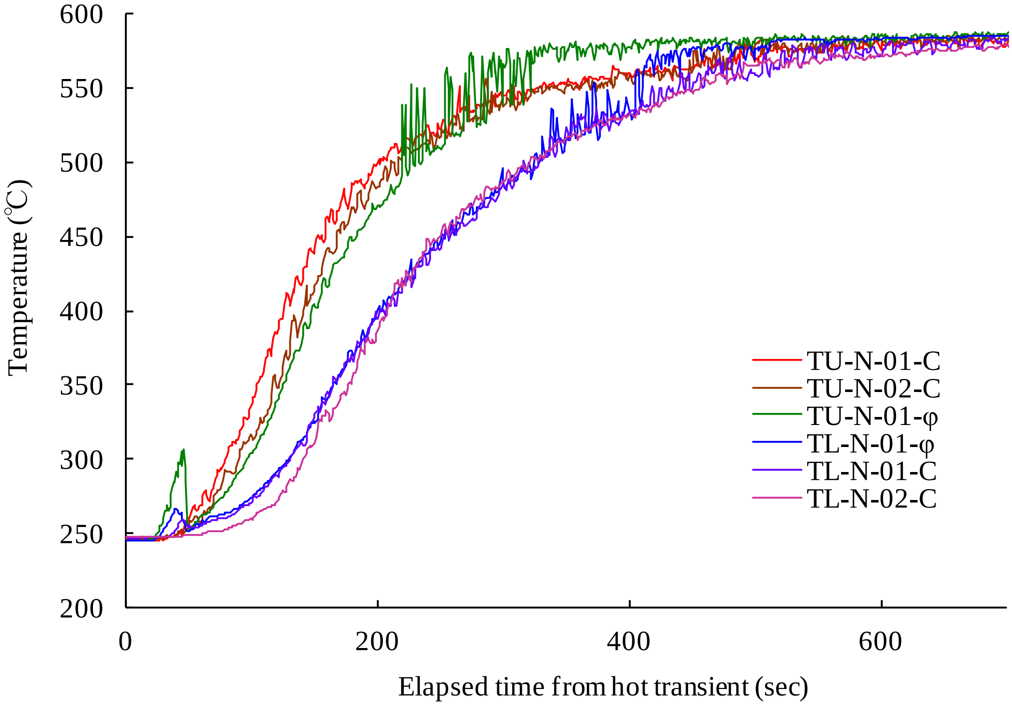

(b) 0 sec ～ 700 sec / cold transient

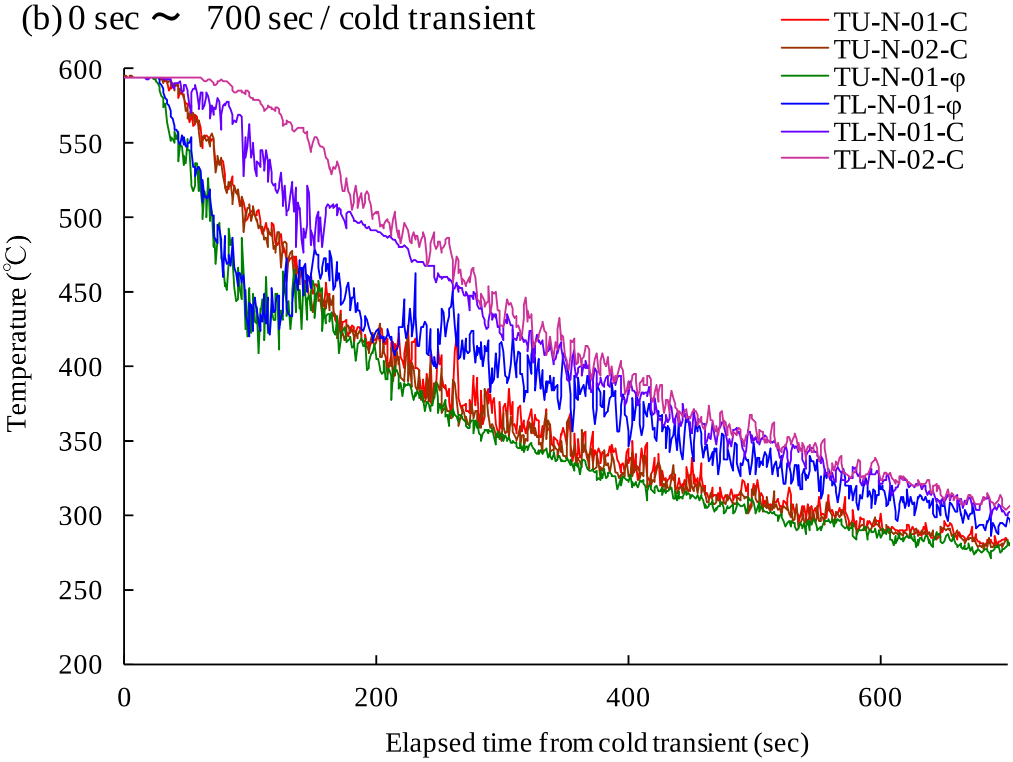

Fig.6

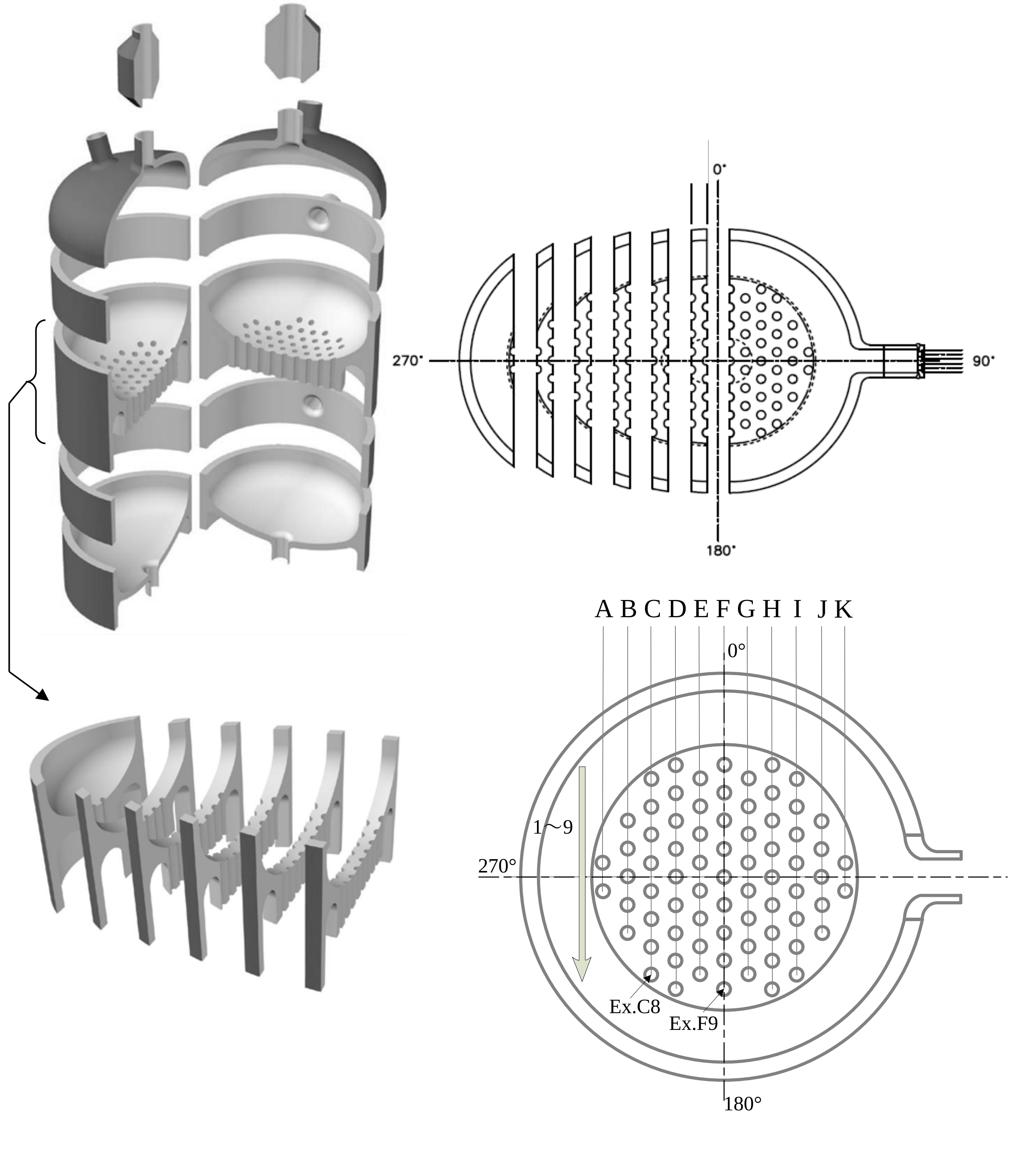

Fig.7

ID	270° side	Upper surface	90° side
A-1	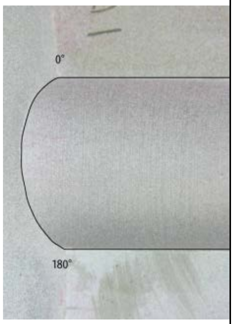	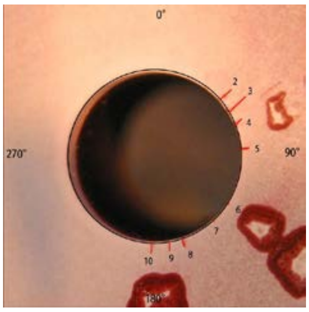	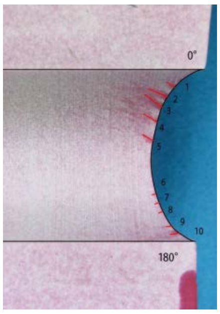
A-2	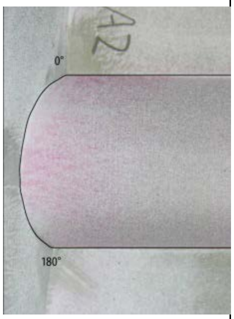	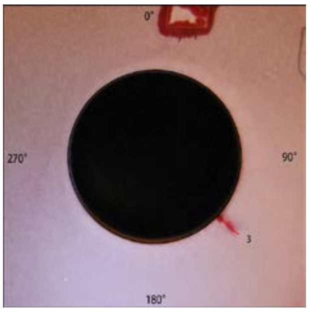	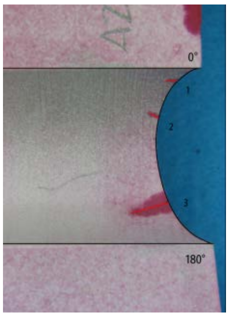
B-1	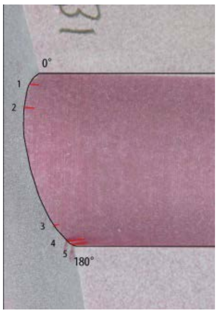	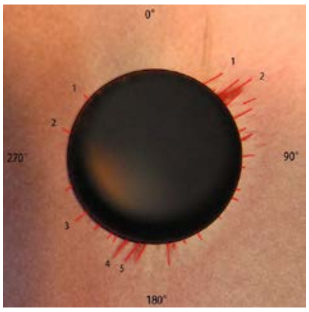	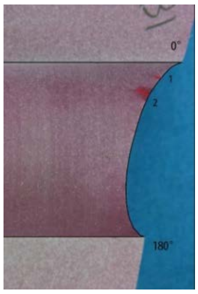
B-2	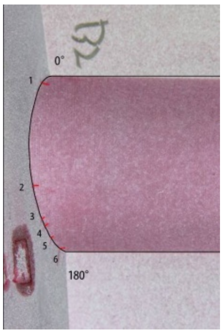	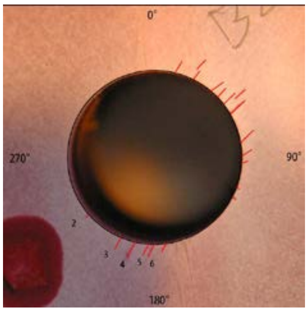	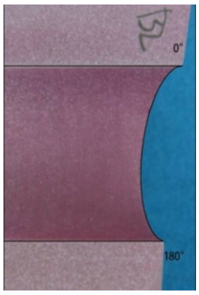

10.0 mm

Fig.8

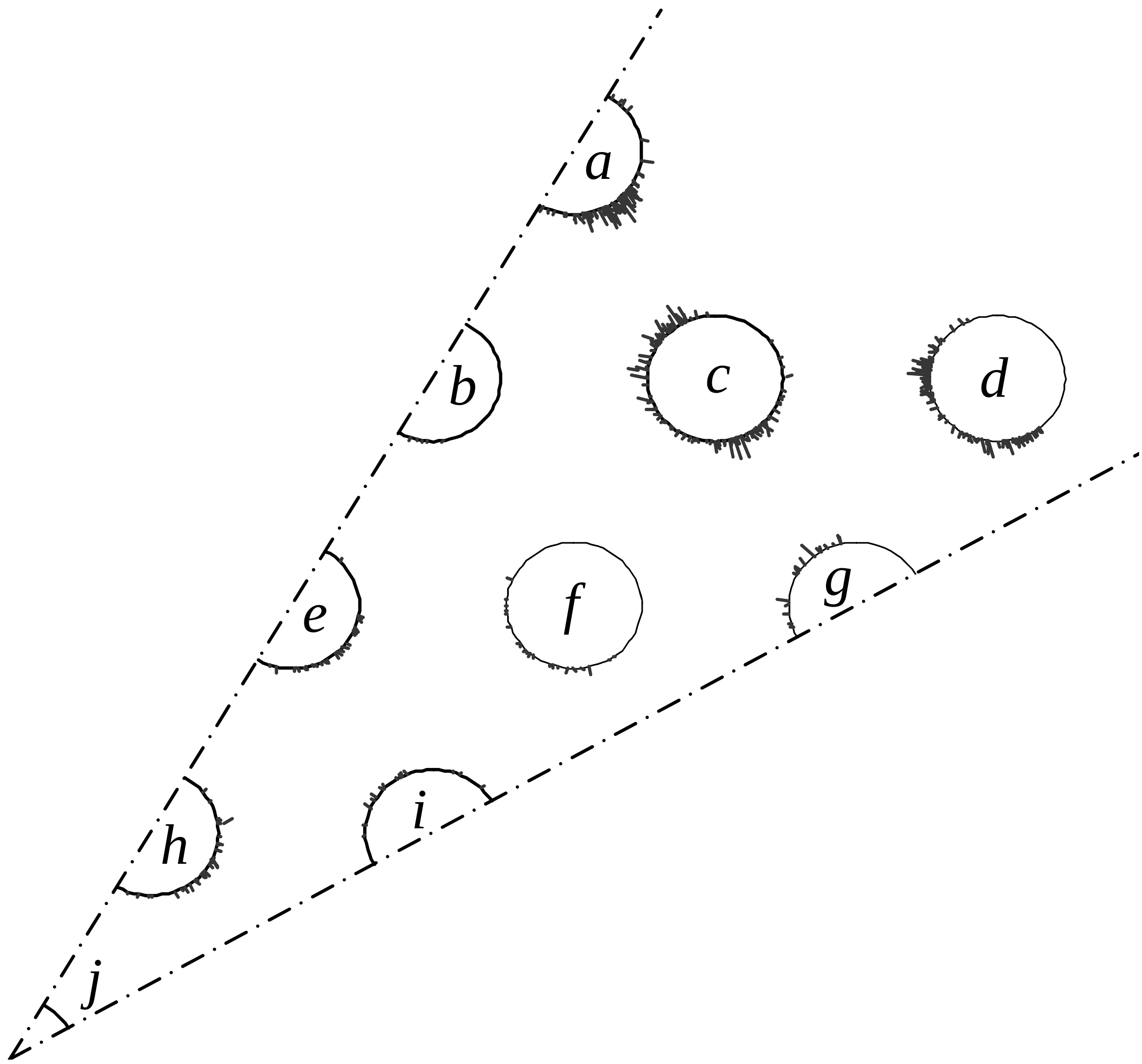

Fig.9

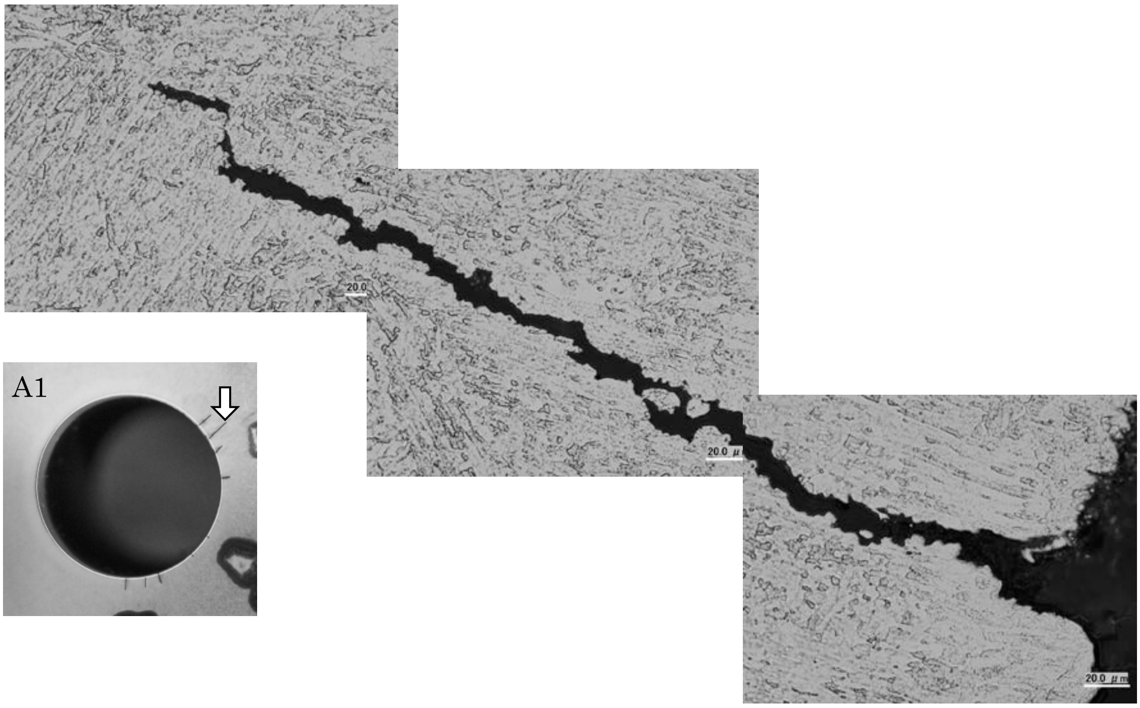

Fig.10

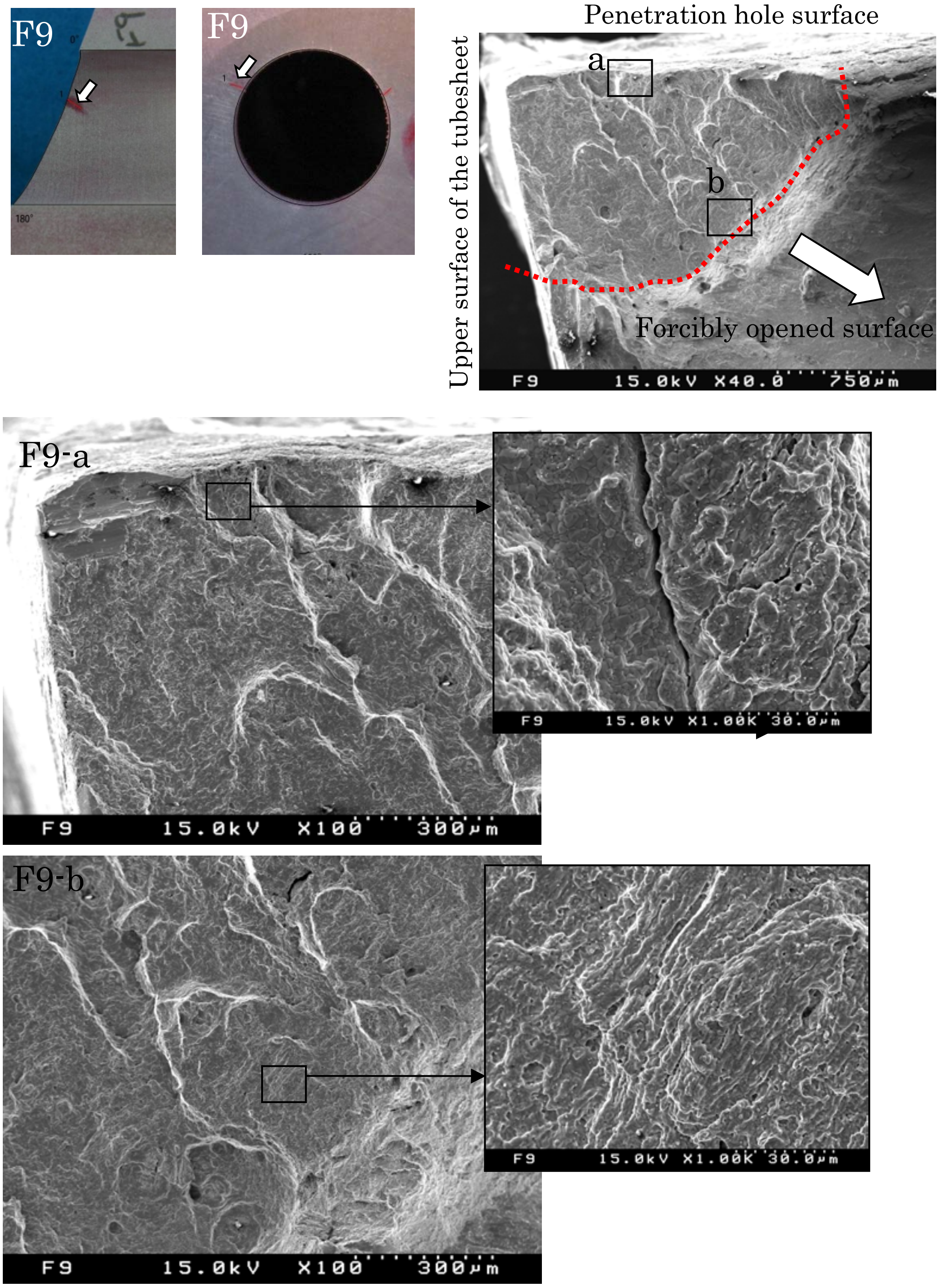
F9
F9
Penetration hole surface
a
b
Upper surface of the tubesheet
Forcibly opened surface
F9 15.0kV X40.0 750μm
F9-a
F9 15.0kV X1.00K 30.0μm
F9 15.0kV X100 300μm
F9-b
F9 15.0kV X1.00K 30.0μm
F9 15.0kV X100 300μm

Fig.11

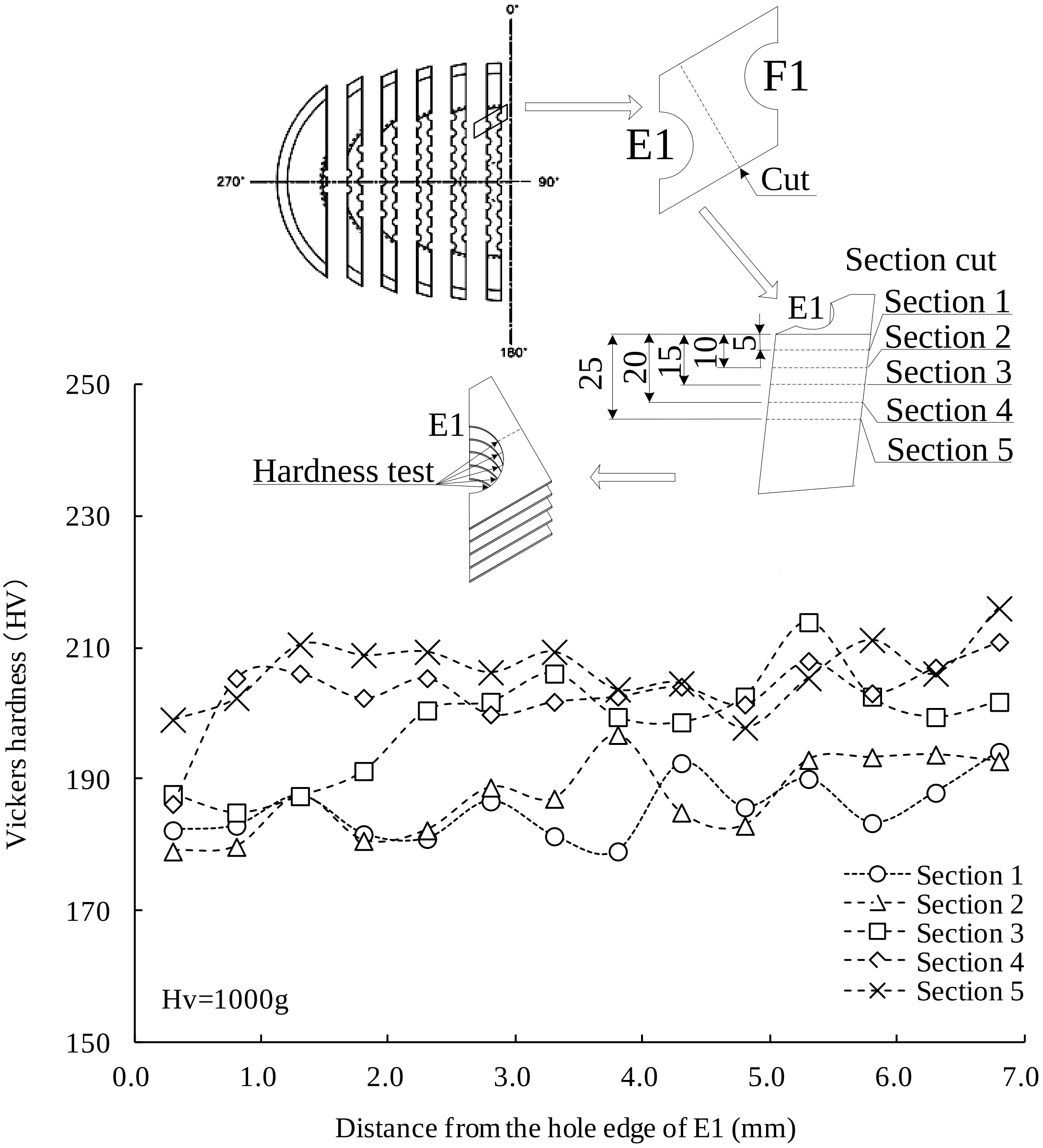

0°
270°
90°
180°
F1
E1
Cut
Section cut
E1
Section 1
Section 2
Section 3
Section 4
Section 5
25
20
15
10
5
E1
Hardness test
250
230
210
190
170
150
Vickers hardness (HV)
0.0
1.0
2.0
3.0
4.0
5.0
6.0
7.0
Distance from the hole edge of E1 (mm)
Section 1
Section 2
Section 3
Section 4
Section 5
Hv=1000g

Fig.12

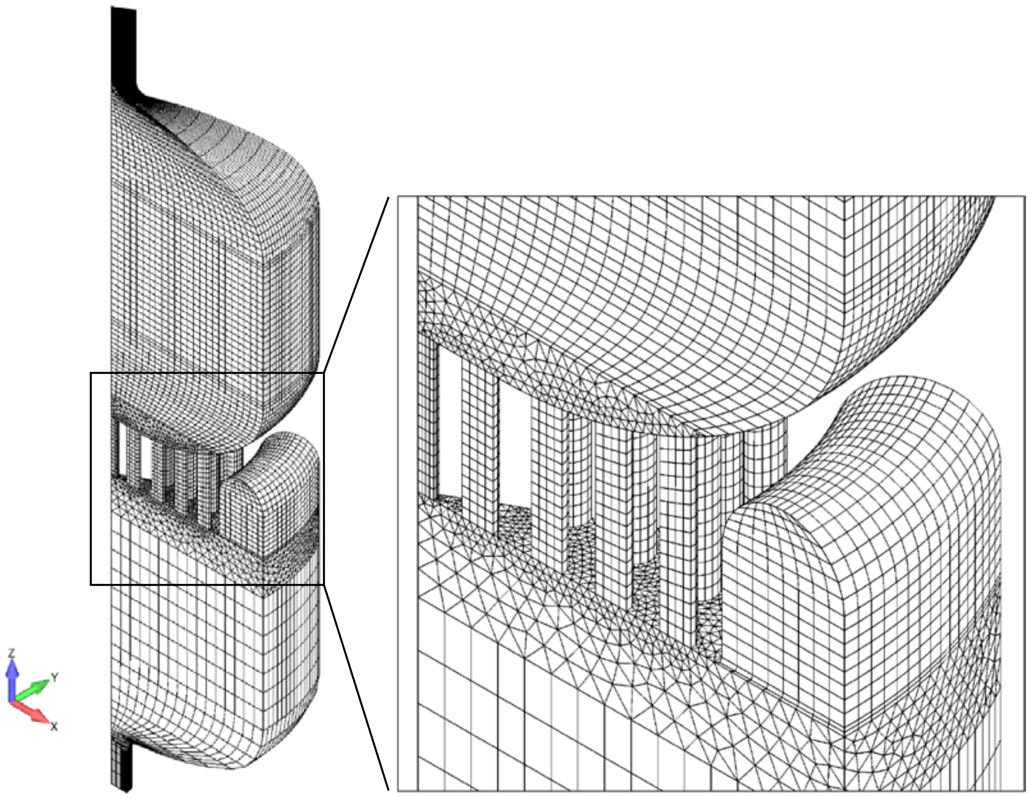

Fig.13

(a) 0 sec ～　700 sec / hot transient

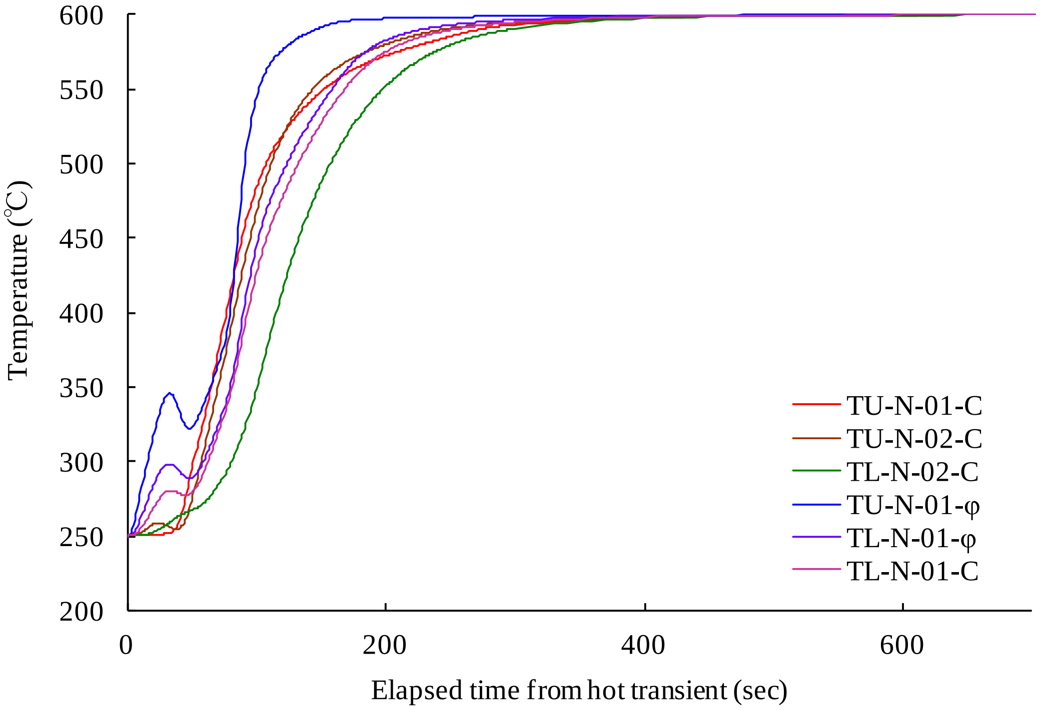

(b) 0 sec ～　700 sec / cold transient

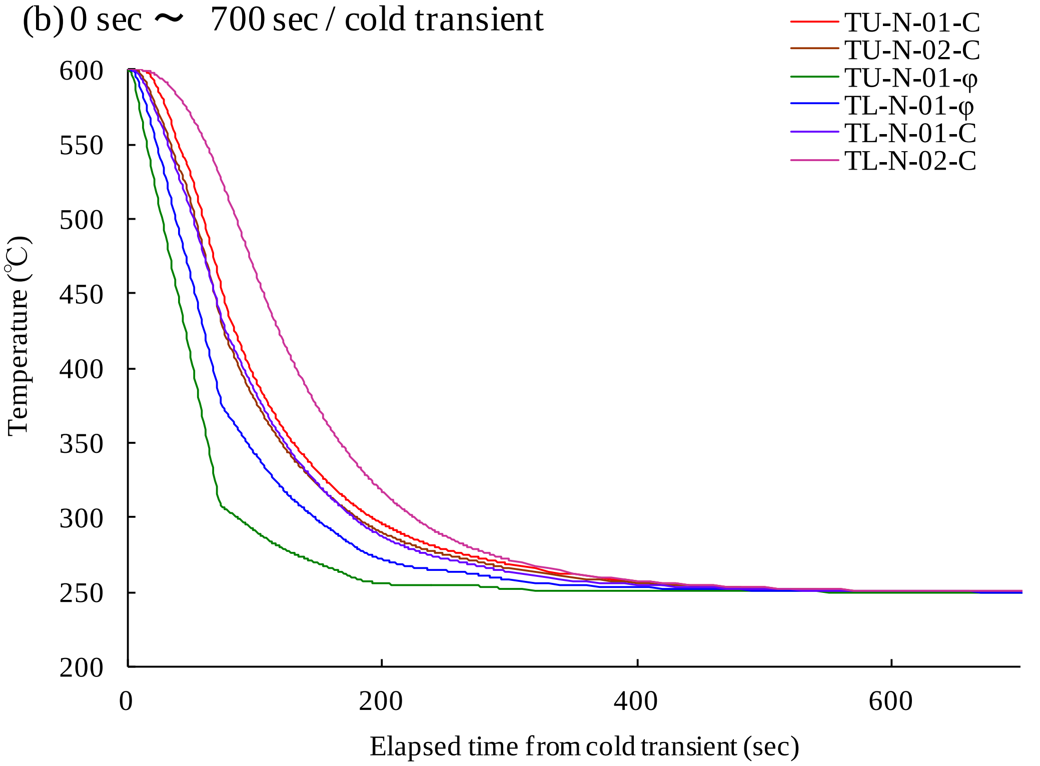

Fig.14

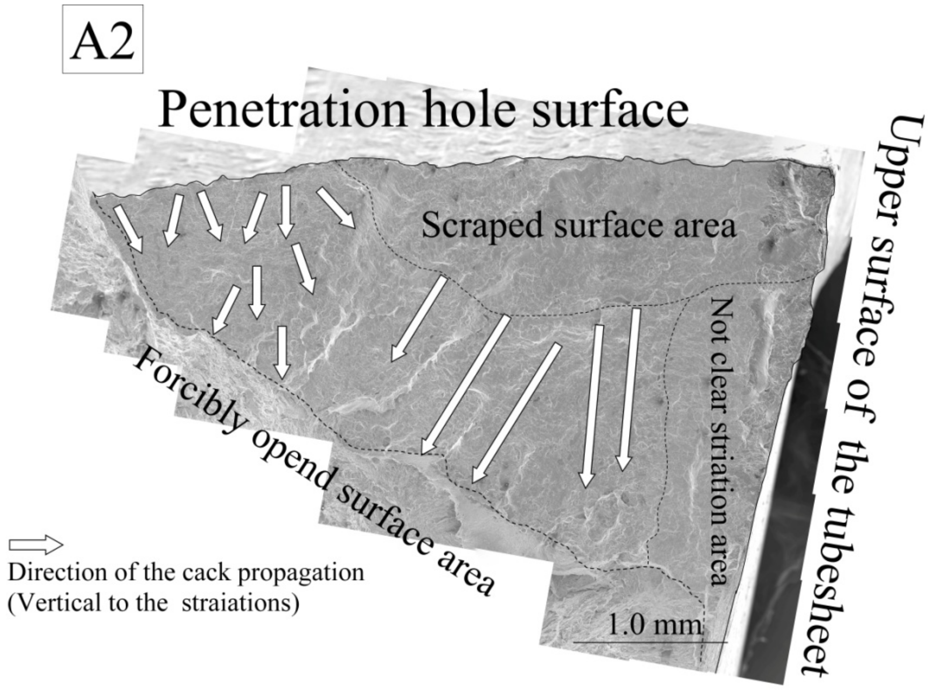
A2
Penetration hole surface
Upper surface of the tubesheet
Scraped surface area
Not clear striation area
Forcibly opend surface area
Direction of the cack propagation
(Vertical to the straiations)
1.0 mm

Fig.15

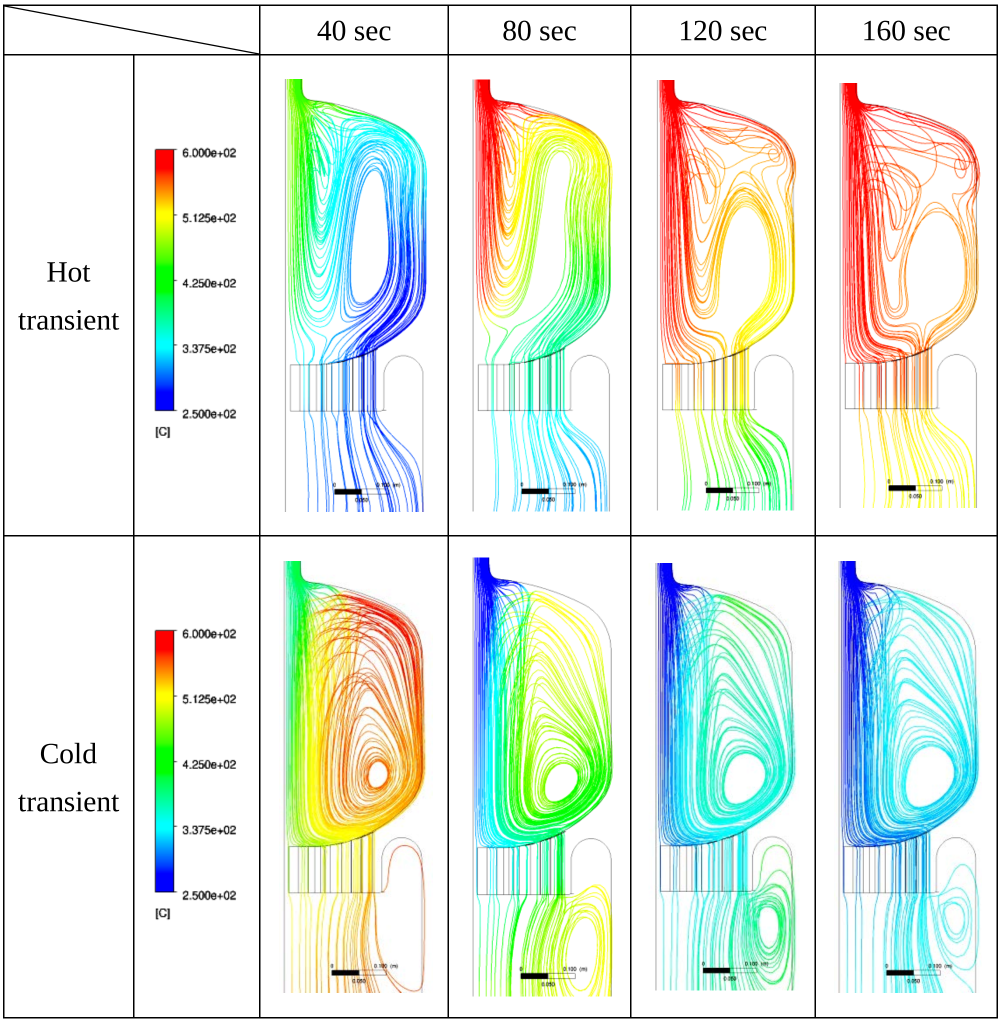
40 sec
80 sec
120 sec
160 sec
Hot
transient
Cold
transient
6.000e+02
5.125e+02
4.250e+02
3.375e+02
2.500e+02
[C]